

Numerical approach to δ -function current sheets arising from resonant magnetic perturbations

Yi-Min Huang,^{1,2,a)} Stuart R. Hudson,² Joaquim Loizu,³ Yao Zhou,² and Amitava Bhattacharjee^{1,2}

¹⁾Department of Astrophysical Sciences, Princeton University, Princeton, New Jersey 08544, USA

²⁾Princeton Plasma Physics Laboratory, Princeton, New Jersey 08543, USA

³⁾École Polytechnique Fédérale de Lausanne, Swiss Plasma Center, CH-1015 Lausanne, Switzerland

General three-dimensional toroidal ideal magnetohydrodynamic equilibria with a continuum of nested flux surfaces are susceptible to forming singular current sheets when resonant perturbations are applied. The presence of singular current sheets indicates that, in the presence of non-zero resistivity, magnetic reconnection will ensue, leading to the formation of magnetic islands and potentially regions of stochastic field lines when islands overlap. Numerically resolving singular current sheets in the ideal MHD limit has been a significant challenge. This work presents numerical solutions of the Hahm-Kulsrud-Taylor (HKT) problem, which is a prototype for resonant singular current sheet formation. The HKT problem is solved by two codes: a Grad-Shafranov (GS) solver and the SPEC code. The GS solver has built-in nested flux surfaces with prescribed magnetic fluxes. The SPEC code implements multi-region relaxed magnetohydrodynamics (MRxMHD), where the solution relaxes to a Taylor state in each region while maintaining force balance across the interfaces between regions. As the number of regions increases, the MRxMHD solution approaches the ideal MHD solution assuming a continuum of nested flux surfaces. We demonstrate excellent agreement between the numerical solutions obtained from the two codes through a thorough convergence study.

I. INTRODUCTION

Ideal magnetohydrodynamics (MHD) permits solutions with singular current sheets.¹ General three-dimensional (3D) ideal MHD equilibria with a continuum of nested flux surfaces, as often assumed by stellarator equilibrium solvers such as VMEC² and NSTAB,³ are susceptible to the formation of singular current sheets at rational surfaces.^{4–6} Nominally two-dimensional (2D) systems such as tokamaks can also develop singular current sheets when subjected to resonant magnetic perturbations (RMPs). The formation of ideal MHD singular current sheets has significant practical implications. With a finite resistivity or other non-ideal effects that enable magnetic reconnection, magnetic field lines surrounding the ideal singular current sheets will break and reconnect, thereby releasing magnetic energy; consequently, the magnetic field will evolve into a field with magnetic islands and possibly regions of stochastic field lines if islands overlap.^{7,8} The sites of ideal MHD singular current sheets, therefore, serve as an indicator of where magnetic reconnection will occur. The intensities of the current sheets also measure the amount of energy available for reconnection.

A prototype for singular current sheet formation driven by RMPs is the Hahm-Kulsrud-Taylor (HKT) problem,^{9–11} shown in Figure 1. This 2D problem has a magnetized plasma enclosed by two conducting walls in a slab geometry. Before the conducting walls are perturbed, the initial magnetic field is a smooth function

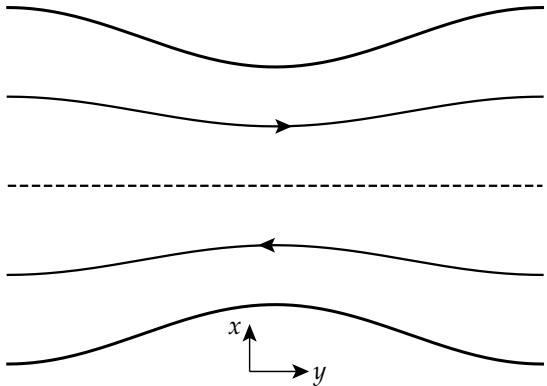


Figure 1. A sketch of the Hahm-Kulsrud-Taylor problem. The in-plane components of the magnetic field reverse directions at the mid-plane (the dashed line). The upper and lower boundaries are shaped by mirror-symmetric sinusoidal perturbations. In response to the perturbation, a singular current sheet develops at the mid-plane.

of space; the in-plane component points along the y direction and B_y reverses direction at the mid-plane (the dashed line in Figure 1); a non-uniform B_z component renders the magnetic field force-free. We then impose a sinusoidal perturbation with an up-down symmetry to the conducting walls and look for a new ideal equilibrium that is consistent with the boundary perturbation while conserves magnetic fluxes between flux surfaces. In this new equilibrium, a singular current sheet will develop at the mid-plane, which is a flux surface that resonates with the boundary perturbation.

The primary objective of this work is to investigate

^{a)}Electronic mail: yimin@princeton.edu

the nature of the ideal HKT singular current sheet by constructing numerical solutions. We limit ourselves to cases of vanishing plasma pressure in this paper, which results in a Dirac δ -function current singularity. For more general cases with a non-vanishing pressure gradient, a Pfirsch–Schlüter current density that diverges algebraically towards the resonant surfaces could arise in addition to the δ -function current singularities.⁶ We leave the Pfirsch–Schlüter current singularity to a future study.

This study employs two numerical codes: (1) a flux conserving Grad–Shafranov (GS) solver¹² and (2) the Stepped Pressure Equilibrium Code (SPEC).¹³

The GS solver assumes a continuum of nested flux surfaces, which precludes magnetic island formation. By prescribing the toroidal (i.e., out-of-plane) and poloidal (i.e., in-plane) fluxes, the geometry of flux surfaces determines the magnetic field. The geometry of the flux surfaces are described by a mapping from a coordinate space to physical space. The numerical implementation discretizes the mapping with a Chebyshev–Fourier pseudospectral method,^{14,15} where the residual MHD force $\mathbf{J} \times \mathbf{B} - \nabla p$ is calculated on a set of collocation points. Here, standard notations are used for the magnetic field (\mathbf{B}), the electric current density (\mathbf{J}), and the plasma pressure (p). The collocation points are uniformly spaced along the Fourier (y) direction and correspond to the interior Chebyshev–Lobato points along the x direction. The mapping is iteratively updated by an energy descent algorithm, similar to that of VMEC, until the residual MHD force is below a threshold. Previously, numerical solutions of the ideal HKT problem from the GS solver have been tested with good agreement against the solutions of a fully Lagrangian solver¹⁶ and analytic solutions obtained with an asymptotic boundary-layer analysis.¹⁷

The SPEC code, on the other hand, solves for multi-region relaxed magnetohydrodynamic (MRxMHD) equilibria.¹³ MRxMHD does not assume a continuum of nested flux surfaces. Instead, the physical domain is divided into nested regions. In each region, the magnetic field relaxes to a Taylor state,¹⁸ i.e., a Beltrami field satisfying the condition $\nabla \times \mathbf{B} = \mu \mathbf{B}$, where μ is a constant, while conserving magnetic helicity as well as the poloidal and the toroidal magnetic fluxes. Force-balance conditions are enforced across the interfaces between adjacent regions. Within each MRxMHD region, formation of magnetic islands and stochastic field line regions is allowed; and the interfaces between MRxMHD regions serve as ideal flux surfaces that prevent the magnetic field from relaxing to a global Taylor state. MRxMHD can be viewed as a bridge between Taylor’s relaxation theory and ideal MHD. When there is only one region in the entire domain, MRxMHD is equivalent to Taylor’s relaxation. On the other hand, in the limit of an infinite number of regions such that the ideal interfaces become a continuum, it has been shown that MRxMHD approaches ideal MHD.¹⁹

We therefore expect SPEC solutions to approach the ideal MHD solution as the number of regions increases.

However, Loizu *et al.*²⁰ previously studied a similar problem of imposing an $m = 2, n = 1$ perturbation on a cylindrical screw pinch with SPEC and concluded that a minimal finite jump, approximately proportional to the perturbation amplitude, in the rotational transform across the resonant surface is a *sine qua non* condition for the existence of a solution. Because the HKT problem has a continuous rotational transform, the *sine qua non* condition raises the question of whether the solutions previously obtained with the fully Lagrangian solver and the GS solver can also be obtained by SPEC. This question was one of the main motivations of this work.

This paper is organized as follows. In Sec. II, we briefly describe the flux preserving formulation of the GS equation and review the linear and nonlinear solutions of the HKT problem. In Sec. III, we present numerical solutions and convergence tests from the GS solver. In Sec. IV, the numerical solutions and convergence tests from SPEC are presented. After thoroughly testing the solutions from the two codes, we further examine the nature of the singular solution in Sec. V. We conclude and discuss future perspectives in Sec. VI.

II. GRAD–SHAFRANOV FORMULATION OF THE HAHM–KULSRUD–TAYLOR PROBLEM

Two-dimensional MHD equilibria in Cartesian geometry satisfy the Grad–Shafranov equation

$$\nabla^2 \psi = -\frac{dP}{d\psi}, \quad (1)$$

where

$$P = p + \frac{B_z^2}{2} \quad (2)$$

is a function of ψ . Here, the Cartesian coordinate z is the direction of translational symmetry. The flux function ψ determines the perpendicular components of the magnetic field through the relation

$$\mathbf{B}_\perp = \hat{\mathbf{z}} \times \nabla \psi. \quad (3)$$

Both the out-of-plane component B_z and the plasma pressure p are functions of ψ . The component B_z is determined by conservation of magnetic flux. In this study, we set p equal to zero.

With the magnetic fluxes prescribed, the magnetic field is determined by the geometry of the flux surfaces. We can label the flux surfaces with an arbitrary variable, and a convenient choice is to use the initial positions x_0 of flux surfaces before the boundary perturbation is imposed. The flux surfaces are described by a mapping from (x_0, y) to (x, y) via a function $x(x_0, y)$. Using the chain rule, we can express the partial derivatives with respect to the Cartesian coordinates in terms of the partial derivatives with respect to the coordinates (x_0, y) :

$$\left(\frac{\partial}{\partial x} \right)_y = \frac{1}{\partial x / \partial x_0} \frac{\partial}{\partial x_0}, \quad (4)$$

$$\left(\frac{\partial}{\partial y}\right)_x = \frac{\partial}{\partial y} - \frac{\partial x/\partial y}{\partial x/\partial x_0} \frac{\partial}{\partial x_0}. \quad (5)$$

Here, the subscripts of the partial derivatives on the left-hand-side indicate the coordinates that are held fixed; the partial derivatives on the right-hand-side are with respect to the (x_0, y) coordinates. Hereafter, partial derivatives are taken to be with respect to the (x_0, y) coordinates by default, unless otherwise indicated by the subscripts.

Using these relations, the Cartesian components of the in-plane magnetic field are given by

$$B_x = - \left(\frac{\partial \psi}{\partial y}\right)_x = \frac{\partial x/\partial y}{\partial x/\partial x_0} \frac{d\psi}{dx_0} \quad (6)$$

and

$$B_y = \left(\frac{\partial \psi}{\partial x}\right)_y = \frac{1}{\partial x/\partial x_0} \frac{d\psi}{dx_0}. \quad (7)$$

The out-of-plane component B_z is determined by conservation of magnetic flux as

$$B_z(x_0) = \frac{B_{z0}(x_0)}{\left\langle \frac{\partial}{\partial x_0} \right\rangle}. \quad (8)$$

Here, B_{z0} is the initial z -component of the magnetic field; the flux surface average $\langle f \rangle$ is defined as

$$\langle f \rangle \equiv \frac{1}{L} \int_0^L f(x_0, y) dy \quad (9)$$

for an arbitrary function $f(x_0, y)$, with $y \in [0, L]$ being the domain of the system along the y direction. The out-of-plane component of the current density is given by

$$J_z = \nabla^2 \psi = \left(\frac{d\psi}{dx_0}\right)^{-1} \frac{\partial}{\partial x_0} \left(\frac{B_x^2 + B_y^2}{2}\right) - \frac{\partial B_x}{\partial y}, \quad (10)$$

and the GS equation can be written as

$$H = - \left(\frac{d\psi}{dx_0}\right)^{-1} \frac{\partial}{\partial x_0} \left(\frac{B_x^2 + B_y^2}{2} + P\right) + \frac{\partial B_x}{\partial y} = 0. \quad (11)$$

The residual MHD force is given by

$$\mathbf{F} \equiv H \nabla \psi. \quad (12)$$

To obtain the solution, we can use $F_x = HB_y$ to push the flux surfaces along the x direction, subjected to a friction force to damp the energy until the system settles to an equilibrium.

For the HKT problem, we consider an initial force-free equilibrium

$$\mathbf{B}_0 = x_0 \hat{\mathbf{y}} + \sqrt{B_0^2 - x_0^2} \hat{\mathbf{z}} \quad (13)$$

in the domain $x_0 \in [-a, a]$ and $y \in [0, L]$, where the y direction is assumed to be periodic. The corresponding in-plane flux function is $\psi = x_0^2/2$. We impose a sinusoidal

perturbation on the boundary that deforms $x = \pm a$ to $x = \pm (a + \delta \cos(ky))$ and let the system evolve under the constraints of ideal MHD to a new equilibrium.

For a small boundary perturbation, we may linearize the GS equation in terms of the displacements of the flux surfaces $\xi(x_0, y) \equiv x(x_0, y) - x_0$. To the leading order in ξ , the magnetic field components are

$$B_x \simeq \frac{\partial \xi}{\partial y} \frac{d\psi}{dx_0}, \quad (14)$$

$$B_y \simeq (1 - \partial \xi / \partial x_0) \frac{d\psi}{dx_0}, \quad (15)$$

and

$$B_z \simeq B_{z0} \left(1 - \left\langle \frac{\partial \xi}{\partial x_0} \right\rangle\right). \quad (16)$$

The linearized GS equation now reads

$$\frac{\partial}{\partial x_0} \left(\left(\frac{d\psi}{dx_0}\right)^2 \frac{\partial \xi}{\partial x_0} + B_{z0}^2 \left\langle \frac{\partial \xi}{\partial x_0} \right\rangle \right) + \frac{\partial^2 \xi}{\partial y^2} \left(\frac{d\psi}{dx_0}\right)^2 = 0. \quad (17)$$

For the HKT problem with $\psi = x_0^2/2$ and the boundary condition $\xi(\pm a, y) = \pm \delta \cos(ky)$, if we adopt the ansatz $\xi = \bar{\xi}(x_0) \cos(ky)$, then $\langle \partial \xi / \partial x_0 \rangle = 0$ and the linearized GS equation reduces to

$$\frac{d^2}{dx_0^2} (x_0 \bar{\xi}) - k^2 x_0 \bar{\xi} = 0. \quad (18)$$

The general solution of Eq. (18) is a linear superposition of two independent solutions

$$\bar{\xi} = c_1 \frac{\sinh(k|x_0|)}{x_0} + c_2 \frac{\cosh(kx_0)}{x_0}, \quad (19)$$

and the boundary condition $\bar{\xi}(\pm a) = \pm \delta$ requires

$$\delta = \frac{c_1 \sinh(ka) + c_2 \cosh(ka)}{a}. \quad (20)$$

We can immediately see that the linear solution is problematic near the resonant surface at $x_0 = 0$. The divergence of $\cosh(kx_0)/x_0$ at $x_0 = 0$ suggests that the coefficient c_2 must be set to zero, and the boundary condition (20) then determines the coefficient $c_1 = a\delta/\sinh(ka)$. However, the limit that $\lim_{x_0 \rightarrow 0} \sinh(k|x_0|)/x_0 = k$ yields $x \simeq x_0 + (ka\delta/\sinh(ka)) \cos(ky)$ in the vicinity of $x_0 = 0$, leading to overlap of flux surfaces when $|x_0| \leq ka\delta/\sinh(ka)$, which amounts to a physical inconsistency and is unpermitted. Therefore, within an inner region $|x_0| \lesssim \mathcal{O}(ka\delta/\sinh(ka))$, the linear solution is not valid and we must consider the nonlinear solution.

The nonlinear solution of the inner region was first derived by Rosenbluth, Dagazian, and Rutherford (hereafter RDR) for the ideal internal kink instability²¹ and

was later adapted to the HKT problem.^{17,22} Because $d\psi/dx_0 \rightarrow 0$ in the inner region, the dominant balance of the GS equation (11) is approximately

$$\frac{\partial}{\partial x_0} \left(\frac{B_y^2}{2} + P(x_0) \right) = 0; \quad (21)$$

here, we have neglected B_x^2 compared to B_y^2 in Eq. (11) by assuming $|\partial x/\partial y| \ll 1$. Integrating Eq. (21) yields

$$B_y = \frac{1}{\partial x/\partial x_0} \frac{d\psi}{dx_0} = \text{sgn} \left(\frac{d\psi}{dx_0} \right) \sqrt{f(x_0) + g(y)}, \quad (22)$$

where

$$f(x_0) = -2P(x_0) + \text{const} \quad (23)$$

and $g(y)$ is an arbitrary function that will be determined later by asymptotic matching to the outer solution; the $\text{sgn}(d\psi/dx_0)$ factor comes from the requirement that $\partial x/\partial x_0 > 0$ must be satisfied to avoid overlapping flux surfaces. Without loss of generality, we are free to set $f(0) = 0$, and the tangential discontinuity of B_y at $x_0 = 0$ is

$$B_y|_{0^\pm} = \pm \sqrt{g(y)}. \quad (24)$$

Using the flux function $\psi = x_0^2/2$ for the HKT problem and integrating Eq. (22) one more time yields the inner solution of RDR

$$x_{RDR}(x_0, y) = \int_0^{x_0} \frac{|x'|}{\sqrt{f(x') + g(y)}} dx'. \quad (25)$$

Note that the functions $f(x_0)$ and $g(y)$ are not independent, but are related through the constraint (23). Here, $P = B_z^2/2$ and B_z is determined by Eq. (8) with $x(x_0, y)$ replaced by $x_{RDR}(x_0, y)$. The resulting relation is cumbersome. To simplify the problem, we further assume that $|B_z| \gg |B_\perp|$ (i.e., in the so-called reduced MHD regime) and replace the constraint (23) by the incompressible constraint $\langle \partial x/\partial x_0 \rangle = 0$, yielding

$$\left\langle \frac{1}{\sqrt{f(x_0) + g(y)}} \right\rangle = \frac{1}{|x_0|}. \quad (26)$$

Once $g(y)$ is obtained, the constraint (26) then determines $f(x_0)$.

The function $g(y)$ can be obtained via asymptotic matching to the linear solution in the outer region. The readers are referred to Ref. [17] for further detail of adapting the matching method of RDR for the internal kink mode to the HKT problem. Here, we simply quote the relevant results. The function $g(y)$ can be obtained by numerically solving an integral equation,²³ but a good analytic approximation for $g(y)$ is

$$g(y) \simeq \frac{4c_1^2 k^2}{3} \sin^8(ky/2), \quad (27)$$

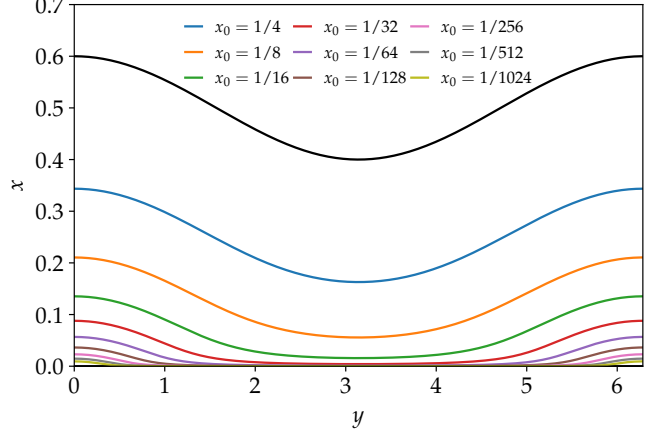


Figure 2. A selection of flux surfaces obtained from the highest resolution calculation that we use as the reference for convergence tests in this study.

where c_1 is the coefficient of the outer solution given by

$$c_1 = \frac{12 \sinh(ka) - \sqrt{144 \sinh^2(ka) - 84\delta k^2 \cosh(ka)}}{7k^2 \cosh(ka)}. \quad (28)$$

III. NUMERICAL SOLUTIONS OF THE GRAD-SHAFRANOV EQUATION

Now we present numerical solutions of the HKT problem obtained by the GS solver. We set the free parameters of this problem to $B_0 = 10$, $a = 1/2$, $\delta = 0.1$, and $k = 2\pi/L = 1$. We assume a mirror symmetry of the solution and solve in only half of the domain $x_0 \in [0, 1/2]$.

We perform two sets of numerical calculations. The first set employs a direct Chebyshev-Fourier pseudospectral discretization of the GS equation. For the second set, we take advantage of the knowledge of RDR's analytic solution and express the geometry of flux surfaces as $x(x_0, y) = x_{RDR}(x_0, y) + \tilde{x}(x_0, y)$. Here, to calculate the analytic solution x_{RDR} , we adopt the analytic approximation (27) for $g(y)$ and numerically solve the incompressible constraint (26) to obtain $f(x_0)$. We then numerically integrate Eq. (25) to obtain x_{RDR} . We rewrite the GS equation in terms of the deviation \tilde{x} from the RDR solution and implement a special version of GS solver for this formulation. Because the analytic solution accounts for most of the singular behavior near the resonant surface, the accuracy of the second set of solutions is substantially improved.

We use $N_y = 512$ collocation points along the y direction to ensure that most of the numerical errors are due to the discretization along the x_0 direction. We then test the convergence of the numerical solution by increasing the number of Chebyshev collocation points N_x . We perform calculations with $N_x = 8, 16, 32, 64$, and 128. The Chebyshev collocation points cluster near the edges of the

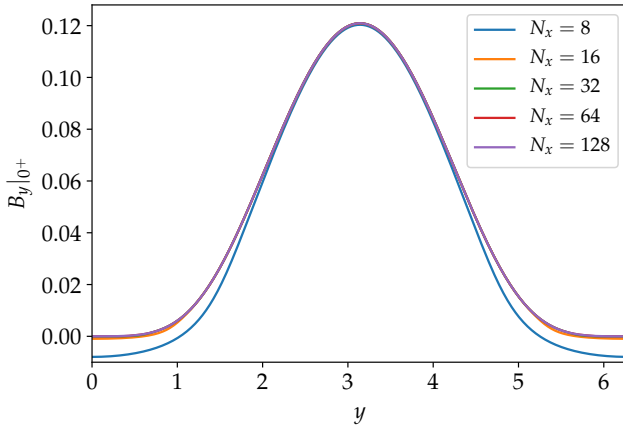


Figure 3. The magnetic field $B_y|_{0+}$ at the lower boundary of the computational domain obtained from the GS solver without RDR subtraction.

domain, with the shortest distance between them scales as $1/N_x^2$. For $N_x = 128$, the closest collocation point is at $x_0 = 7.5 \times 10^{-5}$. Due to the lack of a perfectly precise solution for the convergence test, we take the most accurate numerical solution available as a substitute. For that purpose, the $N_x = 128$ solution from the second set (with the subtraction of the RDR solution) serves as the reference.

Our primary diagnostics for the convergence test are: (a) the discontinuity of magnetic field at the resonant surface $B_y|_{0+}$ ($B_y|_{0-} = -B_y|_{0+}$ from symmetry); and (b) the geometry of a selection of flux surfaces. For the latter, we use the flux surfaces labeled by $x_0 = 1/4, 1/8, 1/16, \dots, 1/1024$. This set of flux surfaces are shown in Fig. 2. We quantify the errors of a solution by the L_2 norms of the differences of relevant quantities relative to the reference solution. Specifically, we use

$$\|\Delta B_y|_{0+}\|_2 \equiv \left\langle \left(B_y|_{0+} - B_y^{ref}|_{0+} \right)^2 \right\rangle^{1/2} \quad (29)$$

and

$$\|\Delta x\|_2 \equiv \left\langle (x - x^{ref})^2 \right\rangle^{1/2}, \quad (30)$$

where the flux surface average is defined in Eq. (9).

The calculation of B_y using Eq. (7) fails at the resonant surface, because both the denominator and the numerator approach zero. To obtain $B_y|_{0+}$, we perform a polynomial extrapolation using the barycentric formula²⁴ with values of B_y on all the collocation points other than $x_0 = 0$. Additionally, because the flux surfaces of choice for the convergence test do not coincide with the Chebyshev collocation points, we have to perform a polynomial interpolation to determine their geometry.

Figure 3 shows $B_y|_{0+}$ from the GS solver with increasing grid resolutions. For $N_x = 8$, we can see that $B_y|_{0+}$ becomes negative near $y = 0$ and $y = 2\pi$. This is a numerical artifact due to discretization and extrapolation errors, as the true solution should remain positive and

only becomes zero at $y = 0$ and $y = 2\pi$. As N_x increases, the solution quickly converges and the curves are virtually on top of one another when $N_x \geq 16$. The values near $y = 0$ and $y = 2\pi$ remain slightly negative, but the magnitude rapidly decreases as N_x increases. For the second set of solutions with RDR subtraction, the curves virtually overlap with each other for all the cases we have done (not shown). Figure 4 shows the convergence of $B_y|_{0+}$ errors for both sets of solutions. We can see that applying RDR subtraction reduces the errors by approximately one order of magnitude, but the overall convergence rates are similar for both sets of solutions.

Likewise, the convergence of flux surface geometry errors is shown in Figure 5 for both sets of solutions. Evidently, flux surfaces closer to the resonant surface are more difficult to solve accurately. Again, the RDR subtraction approximately reduces the errors by an order of magnitude, but the overall convergence rate remains similar.

Note that the data points for $N_x = 128$ with RDR subtraction are missing in Figures 4 and 5, because that solution serves as the reference. The convergence tests provide a base for estimating the errors of the reference solution. Because the same reference solution will also be used for the convergence test of SPEC solutions, it is important to ensure that the reference solution is sufficiently accurate.

The convergence rate of the GS solver is algebraic with respect the number of collocation points, as opposed to the exponential convergence we usually expect from a pseudospectral method, due to the non-smoothness of the solution near the resonant surface (see the discussion in Sec. V). Indeed, when applying to problems without resonant surfaces, the GS solver can achieve an exponential convergence. Although subtracting the RDR solution significantly improves the accuracy of the GS solver, it does not completely remove the effect of the singularity and the convergence rate remains similarly algebraic. The convergence rate could potentially be further improved by adopting a more accurate $g(y)$ in the RDR solution (25), either by numerically solving the RDR integral equation²³ or by dynamically solving $g(y)$ as a part of the solver.

IV. SPEC SOLUTIONS

Now we continue with the SPEC solutions of the HKT problem. Here we also present the results from two sets of numerical calculations. For the first set, the initial positions of interfaces between volumes are uniformly spaced before the boundary perturbation is imposed. We start from the number of volumes $N_{vol} = 2$, then increase to $N_{vol} = 4, 8$, up to $N_{vol} = 128$. For the second set of calculations, the volumes are packed near the resonant surface. We also start from $N_{vol} = 2$. At each level of refinement, the volume adjacent to the resonant surface is divided into two equal volumes. In this way, we go up

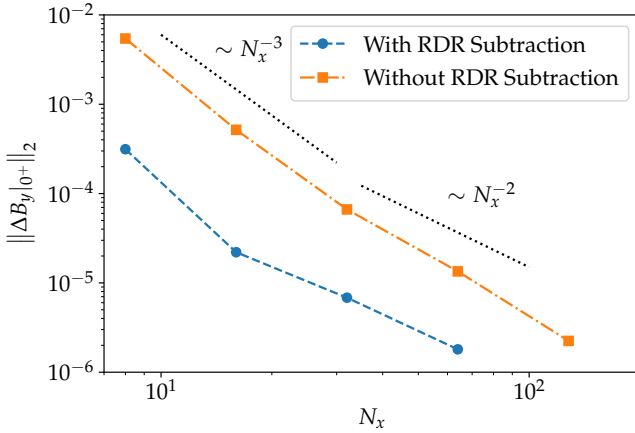


Figure 4. Convergence of $B_y|_{0+}$ errors from the GS solvers with and without subtracting the RDR solution.

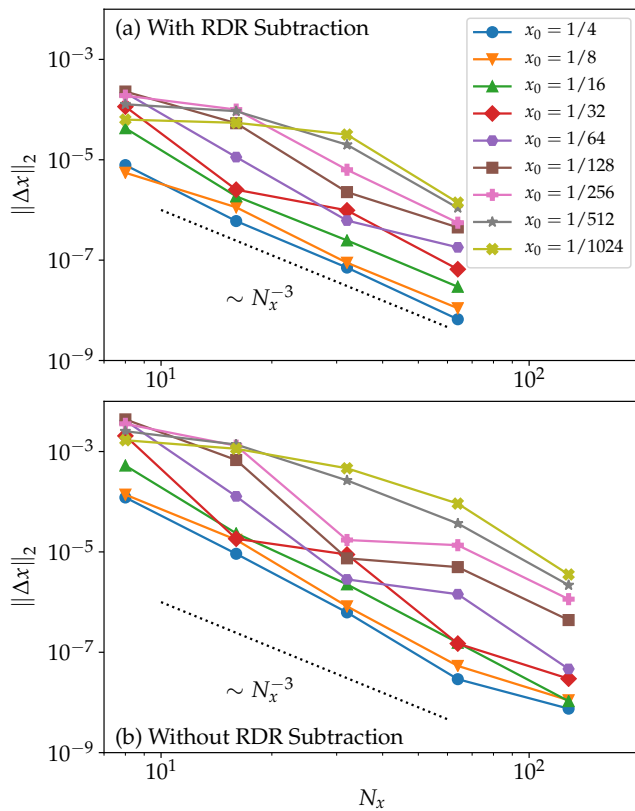


Figure 5. Convergence of flux surface errors from the GS solvers with and without subtracting the RDR solution.

to an “effective” $N_{vol} = 512$, meaning that the smallest volume is $1/512$ of the domain, while the actual number of volumes is $N_{vol} = 10$. The interfaces between volumes for the highest resolution case of the second set exactly correspond to the flux surfaces shown in Fig. 2. We test the convergence of SPEC solutions as the number of volumes increases, using the highest resolution GS solution as the reference. The number of Fourier harmonics along

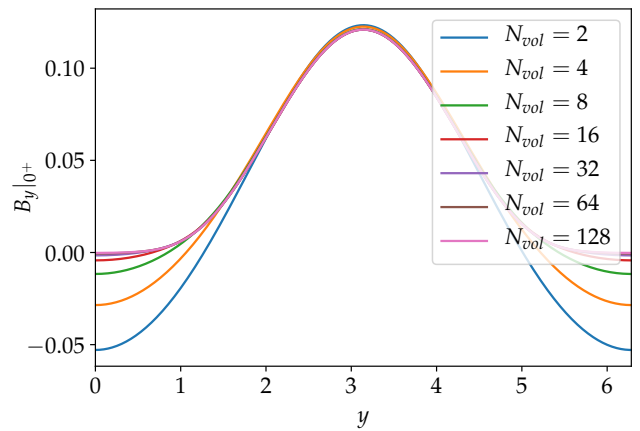


Figure 6. Convergence of $B_y|_{0+}$ of SPEC solutions as the number of uniformly spaced volumes increases.

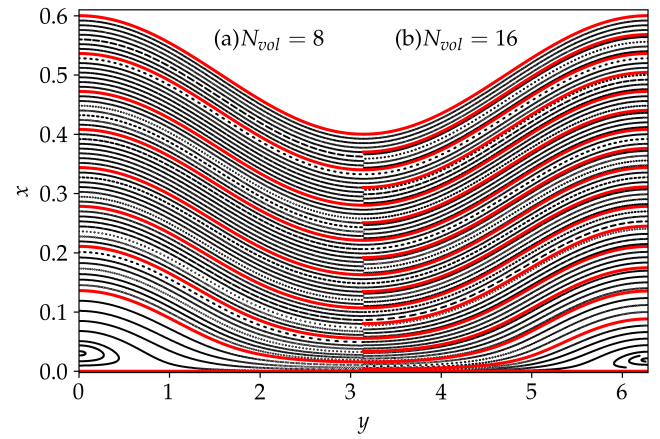


Figure 7. Ideal interfaces between MRxMHD volumes (red) and samples of Poincaré plot in each volumes (black). The left-hand-side shows the case with eight volumes, and the right-hand-side shows the case with sixteen volumes.

the y direction is 48 for all the SPEC calculations presented here.

When SPEC finds a solution, it is not guaranteed that the ideal interfaces between volumes will not overlap with each other. Overlapping ideal interfaces are not permitted on physical grounds, but they do occasionally occur in SPEC solutions, especially for those interfaces close to the resonant surface, and this will cause the SPEC algorithm to crash. Because SPEC uses Newton’s method to find the solution, having a good initial guess is crucial. A useful approach to overcome the problem of overlapping ideal interfaces is to start from a small boundary perturbation, find the solution, then use the solution as the initial guess for a slightly increased boundary perturbation. This process is repeated until the full amplitude of boundary perturbation is reached.

Figure 6 shows $B_y|_{0+}$ from SPEC using uniformly-spaced volumes. Similar to the GS solutions shown in Figure 3, the values of $B_y|_{0+}$ in SPEC solutions also be-

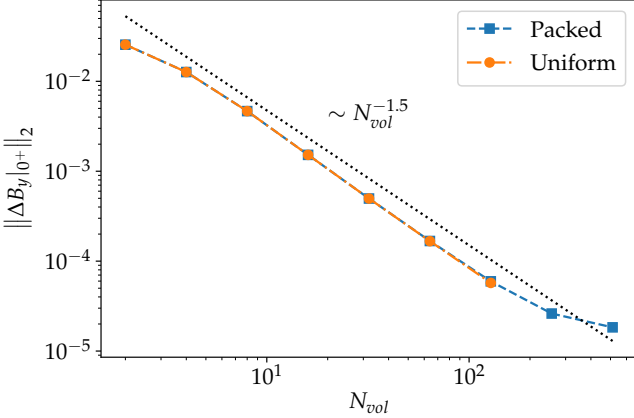


Figure 8. Convergence of the $B_y|_{0+}$ errors of SPEC solutions for cases of packed volume and uniformly-spaced volumes.

come negative near $y = 0$ and $y = 2\pi$, but the magnitude rapidly decreases as the number of volumes increases. The reason for negative $B_y|_{0+}$ is due to the presence of residual magnetic islands near the resonant surface,¹¹ as we can see in Figure 7. Here, the red lines are the ideal interfaces and the black dots represent samples of the Poincaré plot from fieldline tracing. The left-hand-side of the figure shows the $N_{vol} = 8$ case, while the right-hand-side shows the $N_{vol} = 16$ case. The Poincaré plot reveals the residual islands in the lower left and the lower right corners. The size of the island decreases as N_{vol} increases from 8 to 16. This trend continues as N_{vol} further increases, resulting in the decrease of the magnitude of negative $B_y|_{0+}$.

Figure 8 shows the convergence of the errors of $B_y|_{0+}$ as N_{vol} increases, for both sets of SPEC solutions. Here, for the cases of packed volumes, N_{vol} corresponds to the “effective” number of volumes as discussed above. We can see that the errors from both sets are nearly identical for the same N_{vol} , even though the volumes far away from the resonant surface are much coarser for the packed cases. The errors approximately scales as $N_{vol}^{-1.5}$ for both uniform and packed cases. This finding suggests that $B_y|_{0+}$ may not strongly depend on the accuracy in the outer region.

On the other hand, the effects of inadequate resolution in the outer region are evident in the convergence of flux surface errors, shown in Figure 9. Here, the errors consistently scale as N_{vol}^{-3} for cases of uniform volumes. For cases of packed volumes, although the errors initially decrease as N_{vol}^{-3} , the trend eventually flattens as N_{vol} further increases. It is possible that the stalling of convergence in the outer region will eventually affect the convergence of $B_y|_{0+}$ for the packed cases. We can see that the last point of packed cases in Figure 8 exhibits some deviation from the $N_{vol}^{-1.5}$ scaling.

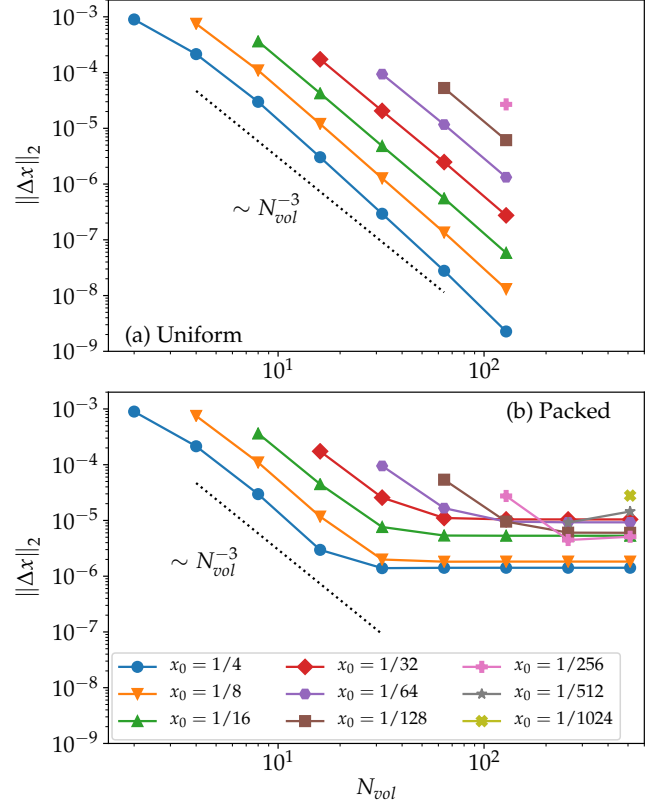


Figure 9. Convergence of the flux surface errors of SPEC solutions. Panel (a) shows the cases of uniformly-spaced volume, and panel (b) shows the cases of packed volumes near the resonant surface.

V. DISCUSSION

The agreement between the GS solver and SPEC provides a solid evidence that both codes are approaching the true solution of the HKT problem as the resolution (or number of volumes) increases. Now we further examine the nature of the singular solution.

The finite tangential discontinuity $B_y|_{0\pm}$ arises from a continuous initial magnetic field through the compression of the space between flux surfaces, which is evident from the flux surfaces shown in Figure 2. As we can infer from the RDR solution (25), for flux surfaces sufficiently close to the resonant surface such that the condition

$$f(x_0) \ll g(y) \quad (31)$$

is satisfied, we have

$$x(x_0, y) \simeq \frac{x_0^2}{\sqrt{g(y)}}. \quad (32)$$

Because $f(0) = 0$ and $g(y) \simeq (4c_1^2 k^2/3) \sin^8(\pi y/L)$, the condition (31) will eventually be satisfied for sufficiently small x_0 for all y except at $y = 0$ and $y = L$, but the transition to the quadratic mapping $x \sim x_0^2$ occurs at different

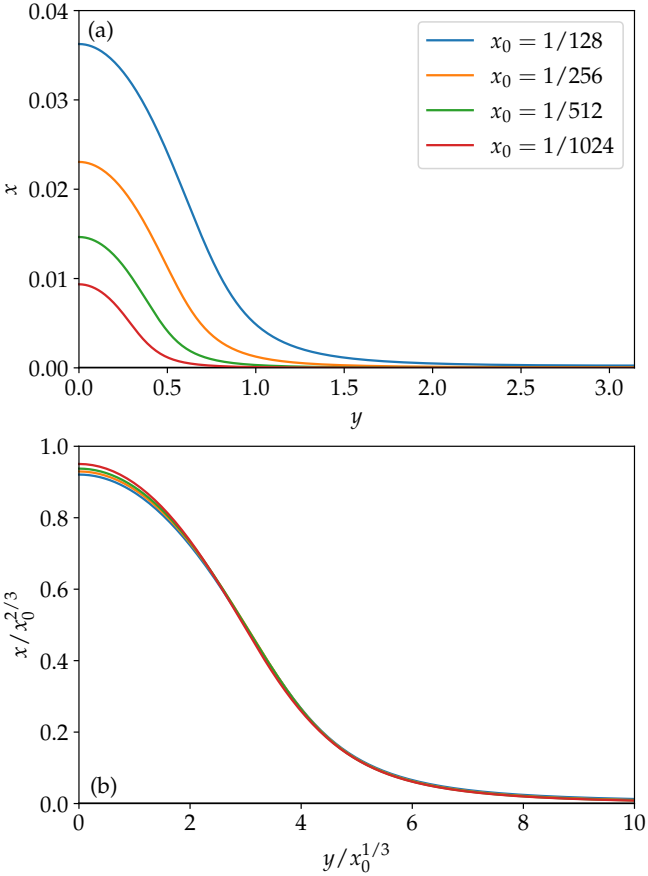


Figure 10. The nested flux surfaces near the resonant surface exhibit a similarity relation. Panel (a) shows a selection of flux surfaces near the lower left corner of Figure 2. After rescaling by $x \rightarrow x/x_0^{2/3}$ and $y \rightarrow y/x_0^{1/3}$, the flux surfaces become nearly identical, as shown in panel (b).

x_0 for different y . To compensate for the strong compression of the quadratic mapping, the “downstream” regions of flux surfaces near $y = 0$ and $y = L$ have to bulge outward to maintain approximate incompressibility.

Now we show that the flux surfaces sufficiently close to the resonant surface satisfy a similarity relation near the downstream region, after a proper rescaling. To reveal the rescaling rules, we first need to establish the behavior of $f(x_0)$ near $x_0 = 0$. When the function $g(y)$ is known, the function $f(x_0)$ can be obtained by solving Eq. (26). Because $f(x_0) \rightarrow 0$ in the limit $|x_0| \rightarrow 0$, the function $1/\sqrt{f(x_0) + g(y)}$ is localized near $y = 0, L$. Hence, in this limit we can approximate $g(y)$ by its leading order

Taylor expansion, yielding

$$\begin{aligned} & \left\langle \frac{1}{\sqrt{f(x_0) + g(y)}} \right\rangle \\ & \simeq \frac{2}{L} \int_0^\infty \frac{dy}{\sqrt{f(x_0) + (4c_1^2 k^2/3)(ky/2)^8}} \\ & = \frac{2}{\pi^{3/2}} \frac{\Gamma(3/8)\Gamma(9/8)}{f(x_0)^{3/8} (4c_1^2 k^2/3)^{1/8}}, \end{aligned} \quad (33)$$

where Γ is the gamma function.²⁵ Plugging Eq. (33) into Eq. (26) yields the leading order behavior of $f(x_0)$ in the limit $|x_0| \rightarrow 0$:

$$f(x_0) \simeq [c_f |x_0|]^{8/3}, \quad (34)$$

where

$$\begin{aligned} c_f & \equiv \frac{2(3/4)^{1/8}}{\pi^{3/2}} \Gamma(3/8)\Gamma(9/8) (c_1 k)^{-1/4} \\ & \simeq 0.7735 (c_1 k)^{-1/4}. \end{aligned} \quad (35)$$

Without loss of generality, here we consider $x_0 \geq 0$. Applying the leading order approximations of $f(x_0)$ and $g(y)$ near $x_0 = 0$ and $y = 0$ to the RDR solution (25) yields

$$x(x_0, y) \simeq \int_0^{x_0} \frac{x'}{\sqrt{d_1 x'^{8/3} + d_2 y^8}} dx', \quad (36)$$

where d_1 and d_2 are some constants. With a change of variables $\zeta = x'/x_0$, equation (36) can be rewritten as

$$\frac{x(x_0, y)}{x_0^{2/3}} \simeq \int_0^1 \frac{\zeta}{\sqrt{d_1 \zeta^{8/3} + d_2 (y/x_0^{1/3})^8}} d\zeta. \quad (37)$$

Equation (37) suggests that if we rescale x and y to $x/x_0^{2/3}$ and $y/x_0^{1/3}$, the flux surfaces near $(x, y) = (0, 0)$ will approximately coincide. This similarity relation is borne out by our numerical solutions, shown in Figure 10 for a selection of flux surfaces before and after rescaling.

The similarity relation implies that the heights of the outbulged flux surfaces in the downstream region scale as $x_0^{2/3}$ and the widths scale as $x_0^{1/3}$; the enclosed volumes scale as x_0 , to be consistent with the incompressible constraint. Therefore, in the limit of $x_0 \rightarrow 0$, the width of the outbulged region becomes narrower and narrower, and eventually approaches a Dirac δ -function $\sim x_0 \delta(y)$.

Examining the solution from a Lagrangian perspective provides further insight to its singular nature. The Lagrangian formulation of ideal MHD describes a state in terms of the mapping from the initial positions \mathbf{x}_0 of fluid elements to their final positions \mathbf{x} . The magnetic field at

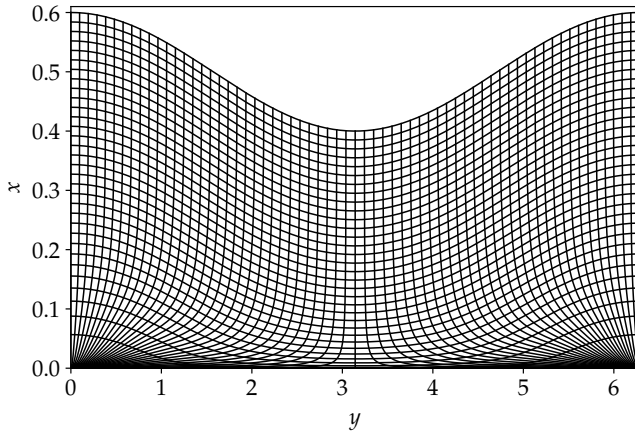


Figure 11. The distorted mesh shows the Lagrangian mapping to the final equilibrium from a rectangular uniform mesh before imposing the boundary perturbation.

\mathbf{x} is determined by the initial magnetic field \mathbf{B}_0 at \mathbf{x}_0 and the mapping $\mathbf{x}(\mathbf{x}_0)$ via the relation^{26,27}

$$\mathbf{B} = \frac{\mathbf{B}_0 \cdot \frac{\partial \mathbf{x}}{\partial \mathbf{x}_0}}{\mathcal{J}}, \quad (38)$$

where $\mathcal{J} = \det(\partial \mathbf{x} / \partial \mathbf{x}_0)$ is the Jacobian of the mapping.

Although our GS solver is not fully Lagrangian because the mesh can move along the x direction but not along the y direction, we can reconstruct the full Lagrangian mapping of fluid elements from the initial to the final state once the solution is obtained. For each fluid element labeled by (x_0, y) in the final solution, we need to find its initial position (x_0, y_0) . This “inverse” Lagrangian mapping can be expressed as a function $y_0(x_0, y)$. From the conservation of magnetic flux through an infinitesimal fluid element

$$B_{z0}(x_0) dx_0 \left[\frac{\partial y_0}{\partial y} dy \right] = B_z(x_0) \left[\frac{\partial x}{\partial x_0} dx_0 \right] dy \quad (39)$$

and using Eq. (8) to relate B_{z0} and B_z , we can calculate

$$\frac{\partial y_0}{\partial y} = \frac{\partial x / \partial x_0}{(\partial x / \partial x_0)} \quad (40)$$

and integrate it along each constant- x_0 contour to obtain $y_0(x_0, y)$.

Figure 11 visualizes how a rectangular uniform mesh in the initial state is deformed by the Lagrangian mapping in the final state. We can see that the mapping is highly distorted near the resonant surface. All the vertical mesh lines in the initial state now converge towards the lower corners in the final state, and the single point $(x_0, y_0) = (0, L/2)$ is stretched to an entire line of the lower boundary. This result strongly suggests that the solution we find here for the HKT problem can only be approached, but can not be reached by ideal MHD evolution described via smooth, diffeomorphic Lagrangian mapping.²⁸

VI. CONCLUSIONS AND FUTURE PERSPECTIVES

In conclusion, we have demonstrated that with the increase of resolution or the number of volumes, the GS solver and SPEC both can converge to the solution of the HKT problem with a δ -function singularity. Our result is also the first to show that SPEC can obtain converged solution of the HKT problem without requiring a discontinuous rotational transform across the resonant surface in the initial condition.

In the previous calculation by Loizu *et al.*,²⁰ the *sine qua non* condition originated from a breakdown of the linear solution near the resonant surface, which was misinterpreted as a lack of a solution. This misunderstanding, compounded with the fact that SPEC uses a Newton method that may fail to find the solution without a carefully chosen initial guess, led to the erroneous conclusion that a finite threshold of discontinuous rotational transform is necessary for the existence of a solution. However, as we have discussed in Sec. II, the breakdown of the linear solution does not imply a lack of a solution, but rather that a nonlinear solution must be sought. Furthermore, by carefully initiating Newton’s method, we have demonstrated that SPEC can obtain the solution. In future work, an energy descent style algorithm will be implemented in SPEC, which should be beneficial for tackling this and similar problems. For instance, one could first use the more robust energy descent algorithm to obtain an approximate solution, then switch to Newton’s method for more rapid convergence to the final solution.

Following up this work, several further investigations will be pursued in the future. Some of the present approach could be adapted to singular current sheets arising from the ideal internal kink instability^{21,29} and more general 3D magnetic resonant perturbations. In addition to the δ -function singularities, the algebraically divergent Pfirsch–Schlüter current in the presence of a pressure gradient should also be investigated. Finally, after the formation of current sheet in real plasmas with non-ideal effects, magnetic reconnection will ensue, forming magnetic islands or regions of stochastic field lines. An important question of practical significance is whether the sizes of saturated islands or regions of stochastic field lines can be predicted from the intensity of current singularities.^{5,30} If such a relationship can be established, we may use singularity intensities as a proxy in for the sizes of magnetic island (or regions of stochastic field lines) in stellarator optimization.

ACKNOWLEDGMENTS

This research was supported by the U.S. Department of Energy under Contract No. DE-AC02-09CH11466 and by a grant from the Simons Foundation/SFARI (560651, AB). Part of this work has been carried out within the framework of the EUROfusion Consortium and has received funding from the Euratom research and train-

ing programme 2014–2018 and 2019–2020 under Grant Agreement No. 633053. The views and opinions expressed herein do not necessarily reflect those of the European Commission.

DATA AVAILABILITY

The data that support the findings of this study are available from the corresponding author upon reasonable request.

REFERENCES

- ¹E. N. Parker, *Spontaneous Current Sheets in Magnetic Fields* (Oxford University Press, Inc., 1994).
- ²S. P. Hirshman and J. C. Whitson, *Physics of Fluids* **26**, 3553 (1983).
- ³P. R. Garabedian, *Proceedings of the National Academy of Sciences* **99**, 10257 (2002).
- ⁴H. Grad, *Phys. Fluids* **10**, 137 (1967).
- ⁵A. Bhattacharjee, T. Hayashi, C. C. Hegna, N. Nakajima, and T. Sato, *Phys. Plasmas* **2**, 883 (1995).
- ⁶P. Helander, *Reports on Progress in Physics* **77**, 087001 (2014).
- ⁷D. Biskamp, *Nonlinear Magnetohydrodynamics* (Cambridge University Press, 1993).
- ⁸D. Biskamp, *Magnetic Reconnection in Plasmas* (Cambridge University Press, 2000).
- ⁹T. S. Hahm and R. M. Kulsrud, *Phys. Fluids* **28**, 2412 (1985).
- ¹⁰X. Wang and A. Bhattacharjee, *Phys. Fluids B* **4**, 1795 (1992).
- ¹¹R. L. Dewar, S. R. Hudson, A. Bhattacharjee, and Z. Yoshida, *Phys. Plasmas* **24**, 042507 (2017).
- ¹²Y.-M. Huang, A. Bhattacharjee, and E. G. Zweibel, *Astrophys. J. Lett.* **699**, L144 (2009).
- ¹³S. R. Hudson, R. L. Dewar, G. Dennis, M. J. Hole, M. McGann, G. von Nessi, and S. Lazerson, *Physics of Plasmas* **19**, 112502 (2012).
- ¹⁴B. Fornberg, *A Practical Guide to Pseudospectral Methods* (Cambridge University Press, 1995).
- ¹⁵L. N. Trefethen, *Spectral Methods in Matlab* (SIAM Philadelphia, 2000).
- ¹⁶Y. Zhou, Y.-M. Huang, H. Qin, and A. Bhattacharjee, *Phys. Rev. E* **93**, 023205 (2016).
- ¹⁷Y. Zhou, Y.-M. Huang, A. H. Reiman, H. Qin, and A. Bhattacharjee, *Physics of Plasmas* **26**, 022103 (2019).
- ¹⁸J. B. Taylor, *Phys. Rev. Lett.* **33**, 1139 (1974).
- ¹⁹G. R. Dennis, S. R. Hudson, R. L. Dewar, and M. J. Hole, *Physics of Plasmas* **20**, 032509 (2013).
- ²⁰J. Loizu, S. R. Hudson, A. Bhattacharjee, S. Lazerson, and P. Helander, *Physics of Plasmas* **22**, 090704 (2015).
- ²¹M. N. Rosenbluth, R. Y. Dagazian, and P. H. Rutherford, *Phys. Fluids* **16**, 1894 (1973).
- ²²A. H. Boozer and N. Pomphrey, *Physics of Plasmas* **17**, 110707 (2010).
- ²³J. Loizu and P. Helander, *Phys. Plasmas* **24**, 040701 (2017).
- ²⁴J.-P. Berrut and L. N. Trefethen, *SIAM Review* **46**, 501 (2004).
- ²⁵M. Abramowitz and I. A. Stegun, eds., *Handbook of Mathematical Functions with Formulas, Graphs, and Mathematical Tables*, 10th ed. (National Bureau of Standards, 1972).
- ²⁶W. A. Newcomb, *Nuclear Fusion Supplement, Part 2*, 451 (1962).
- ²⁷Y. Zhou, H. Qin, J. W. Burby, and A. Bhattacharjee, *Phys. Plasmas* **21**, 102109 (2014).
- ²⁸D. Pfefferl  , L. Noakes, and Y. Zhou, *Plasma Physics and Controlled Fusion* **62**, 074004 (2020).
- ²⁹W. Park, D. A. Monticello, R. B. White, and S. C. Jardin, *Nucl. Fusion* **20**, 1181 (1980).
- ³⁰J. Loizu, Y.-M. Huang, S. R. Hudson, A. Baillod, A. Kumar, and Z. S. Qu, *Physics of Plasmas* **27**, 070701 (2020).